LES of an asymmetrically heated high aspect ratio duct at high reynolds number at different wall temperatures

Kaller, Thomas; Hickel, Stefan; Adams, Nikolaus A.

DOI
10.2514/6.2018-4287

Publication date
2018

Document Version
Accepted author manuscript

Published in
2018 Joint Thermophysics and Heat Transfer Conference

LES of an Asymmetrically Heated High Aspect Ratio Duct at High Reynolds Number at Different Wall Temperatures

Thomas Kaller[1], Stefan Hickel[2] and Nikolaus A. Adams[3]
[1,3]*Technical University of Munich, Department of Mechanical Engineering, 85748 Garching, Germany*
[2]*Technische Universiteit Delft, Faculty of Aerospace Engineering, 2629 HS Delft, The Netherlands*

We present the results of well-resolved large-eddy simulations (LES) of an asymmetrically heated high aspect ratio cooling duct (HARCD) with an aspect ratio of $AR = 4.3$ for two different wall temperatures. The temperature difference with respect to the bulk flow is $\Delta T = 40\,\mathrm{K}$, respectively $\Delta T = 60\,\mathrm{K}$. The HARCD is operated with liquid water at a Reynolds number of $Re_b = 110 \cdot 10^3$ based on bulk velocity and hydraulic diameter. The generic HARCD setup follows a reference experiment. The main goal of the present study is the numerical investigation of the interaction of turbulent heat transfer and the turbulent duct flow, specifically the heating induced changes in mean flow and turbulent statistics with a spatially growing temperature boundary layer. Furthermore, we investigate the influence of asymmetric wall heating on streamwise vorticity and its dynamics as well as the turbulent Prandtl number and the effect of the secondary flow on its distribution.

Nomenclature

$[L_x, L_y, L_z]$ = dimensions in x-,y- and z-direction
d_h = hydraulic diameter
AR = duct aspect ratio
$[u, v, w]$ = velocity components in x-,y- and z-direction
p = pressure
ρ = density
T = temperature
ν = kinematic viscosity
Re = Reynolds number
Re_τ = friction Reynolds number
Nu = Nusselt number
Pr = Prandtl number
Pr_t = turbulent Prandtl number
ϵ_M = turbulent eddy viscosity
ϵ_H = turbulent eddy diffusivity
τ_w = wall shear stress
u_τ = friction velocity
per = index for the periodic section
$heat$ = index for the heated section
b = index for bulk quantities
w = index for wall quantities
$\overline{(\cdot)}$ = temporally averaged value
$(\cdot')$ = fluctuating value
$(\cdot^+)$ = value non-dimensionalized with the friction velocity u_τ

[1]Research Associate, Technical University of Munich, Institute of Aerodynamics and Fluid Mechanics, Boltzmannstr. 15, 85748 Garching, Germany
[2]Full Professor, Technische Universiteit Delft, Faculty of Aerospace Engineering, Kluyverweg 1, 2629 HS Delft, The Netherlands
[3]Full Professor, Technical University of Munich, Institute of Aerodynamics and Fluid Mechanics, Boltzmannstr. 15, 85748 Garching, Germany. Member AIAA

I. Introduction

Turbulent flow through rectangular ducts of high aspect ratio including asymmetrical heat transfer is of great interest for many engineering applications. Typical examples are building ventilation systems, cooling ducts in motors of hybrid electrical vehicles or rocket engine cooling systems. A detailed understanding of cooling duct flows is required for predicting the cooling capability of the respective system in the design process.

The turbulent duct flow and heat transfer is strongly influenced by the presence of secondary flows. The literature distinguishes two main classes of secondary flows: the so-called Prandtl's flow of the first kind induced by the curvature of the geometry and the associated pressure gradient and the turbulence-induced Prandtl's flow of the second kind. A better understanding can be obtained using the streamwise vorticity equation

$$\overbrace{\overline{u}\frac{\partial\overline{\omega}_x}{\partial x}+\overline{v}\frac{\partial\overline{\omega}_x}{\partial y}+\overline{w}\frac{\partial\overline{\omega}_x}{\partial z}}^{T_{\overline{\omega}_x,conv}}=\overbrace{\nu\left(\frac{\partial^2\overline{\omega}_x}{\partial x^2}+\frac{\partial^2\overline{\omega}_x}{\partial y^2}+\frac{\partial^2\overline{\omega}_x}{\partial z^2}\right)}^{T_{\overline{\omega}_x,visc}}$$
$$+\underbrace{\overline{\omega}_x\frac{\partial\overline{u}}{\partial x}+\overline{\omega}_y\frac{\partial\overline{u}}{\partial y}+\overline{\omega}_z\frac{\partial\overline{u}}{\partial z}}_{T_{\overline{\omega}_x,stretch/tilt}}+\underbrace{\left(\frac{\partial^2}{\partial z^2}-\frac{\partial^2}{\partial y^2}\right)\left(\overline{v'w'}\right)}_{T_{\overline{\omega}_x,turb,1}}+\underbrace{\frac{\partial^2}{\partial y\partial z}\left(\overline{v'v'}-\overline{w'w'}\right)}_{T_{\overline{\omega}_x,turb,2}}, \tag{1}$$

where the mean streamwise vorticity is defined as $\overline{\omega}_x = \partial\overline{w}/\partial y - \partial\overline{v}/\partial z$. A detailed analysis of equation 1 can be found e.g. in [1] and [2]. The term $T_{\overline{\omega}_x,conv}$ describes the convective transport of mean streamwise vorticity and $T_{\overline{\omega}_x,visc}$ on the right hand side is the viscous diffusion term. $T_{\overline{\omega}_x,stretch/tilt}$ denotes the vortex stretching and tilting by the mean velocity gradient being the source of the Prandtl's flow of the first kind. $T_{\overline{\omega}_x,turb,1}$ comprises the gradients of the Reynolds shear stress component $\overline{v'w'}$ and $T_{\overline{\omega}_x,turb,2}$ the gradient of the difference of the cross-section Reynolds normal stresses $\overline{v'v'}$ and $\overline{w'w'}$. The last two terms form the source term for the Prandtl's flow of the second kind. For our case of a fully developed turbulent flow through a straight duct $T_{\overline{\omega}_x,stretch/tilt}$ equals zero and only the turbulence-induced secondary flow is present. As a consequence of the anisotropy of the Reynolds stress tensor a pair of counter-rotating streamwise vortices forms in each duct corner. In comparison with the curvature induced-secondary flow, the turbulence-induced secondary flow is relatively weak with $1-3\%$ of the bulk velocity u_b. Nonetheless, the vortices increase the mixing and thus exhibit a significant influence on momentum and temperature transport.

Several experimental and numerical studies have investigated duct flows of different cross-section. First detailed measurements in square ducts were done by i.e. [3], [4] and [5]. The influence of wall heating was analyzed by [6] for a channel flow. [7] studied the flow through an adiabatic high aspect ratio duct with $AR = 11.7$. A first LES of a square duct flow was presented by [8] and direct numerical simulations (DNS) by [2] and [9]. [10] studied the influence of wall heating on the turbulent duct flow. [11] extended this work to the investigation of the spacial development of the flow field along a heated square duct. [12] performed a DNS for a heated square duct with the main focus on the interaction of turbulence- and buoyancy-driven secondary flow. All mentioned numerical studies were conducted at relatively low Reynolds numbers. [13] presented coarse DNS of a heated duct for $Re_b = 10^4$ to $Re_b = 10^6$, however at a relatively low spatial resolution. Recently [14] studied adiabatic duct flow via DNS for a range of Reynolds numbers up to $Re_b = 40 \cdot 10^3$ with a focus on the Reynolds number dependence of mean and secondary flow. All previous publications used a square duct cross-section, investigations for rectangular duct flows, especially for high aspect ratios are much scarcer in the literature. [15] analyzed the turbulent heat transfer for rectangular ducts with moderate aspect ratios ranging from $AR = 0.25$ to $AR = 1.5$. [16] presented DNS of adiabatic periodic duct flows for various aspect ratios ranging from $AR = 1$ to $AR = 7$. Both studies have been conducted at a much lower Reynolds number than the present study.

In the present work, we investigate the influence of asymmetrical turbulent heat transfer on the flow field of a high aspect ratio cooling duct with $AR = 4.3$ at a Reynolds number of $Re_b = 110 \cdot 10^3$ with a well-resolved LES. Two cases at different wall temperatures of $\Delta T = T_w - T_b = 40\,\mathrm{K}$ and $\Delta T = 60\,\mathrm{K}$ are considered. The main focus is the investigation of the spatially developing temperature boundary layer and its effect on the turbulent duct flow field. Our study is motivated by the lack of data for such a configuration. First, the used numerical model and the simulation setup including the experiment is described. As part of the results section a comparison of numerical and experimental results follows. We then continue with the analysis of the turbulent duct flow field, subdivided into three parts: The investigation of the mean flow field including the spatial development of the temperature field, the streamwise vorticity distribution and its dynamics and the turbulent Prandtl number distribution.

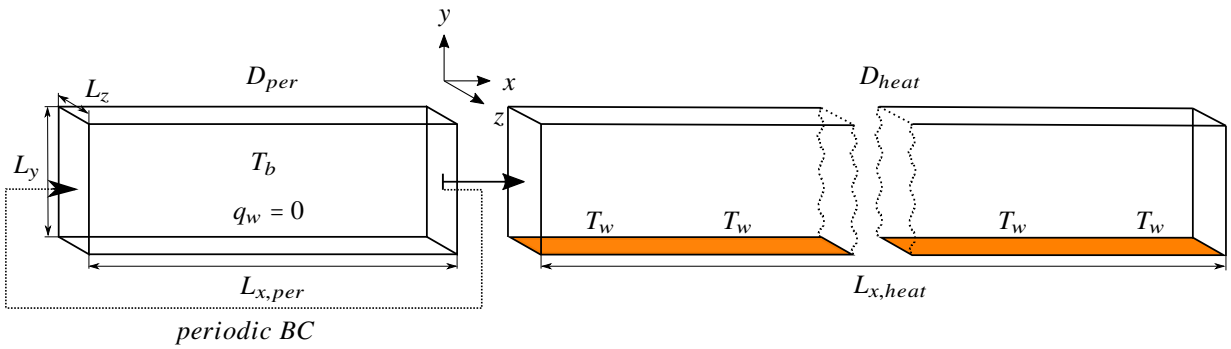

Fig. 1 Sketch of the numerical cooling duct setup, reproduced from [22].

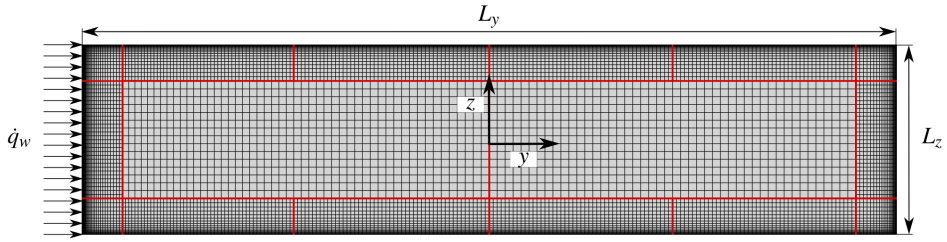

Fig. 2 Used grid in the duct cross-section (every 2nd grid line shown), reproduced from [22].

II. Numerical Model

The flow is described by the incompressible Boussinesq equations as the density variations are relatively small. The temperature is treated as an active scalar and the temperature and density dependent thermodynamic properties of the fluid, i.e. the viscosity and thermal conductivity, are obtained using the IAPWS correlations, see [17] and [18].

The system of equations is discretized by a fractional step finite-volume method on a block structured, staggered Cartesian grid. An explicit third-order Runge-Kutta scheme is applied as time advancement method and the time-step is dynamically adjusted to maintain a maximum Courant number of 1.0.

For the discretization of the pressure Poisson equation as well as the diffusive fluxes we use a second-order accurate central difference scheme. The pressure Poisson equation is solved in every Runge-Kutta substep using a Krylov subspace solver with an algebraic-multigrid preconditioner for convergence acceleration. For discretizing the convective fluxes the Adaptive Local Deconvolution Method (ALDM) is used, respectively the computationally more efficient simplified adaptive local deconvolution (SALD) method. ALDM is a nonlinear finite volume method that provides a physically consistent subgrid-scale turbulence model for implicit LES, see [19] and [20]. For the extension of ALDM to scalar mixing see [21]

III. Simulation Setup

The LES simulation follows closely the experimental setup of a high aspect ratio water cooling duct by project partners presented in [23]. At the beginning of the closed loop test stand water flows at a constant flow rate of 50 l/min and a temperature of $T_b = 333.15\,\mathrm{K}$ from a reservoir through an unheated feed line of 600 mm. Between feed line and the equally long 600 mm heated test section a flow straigthener is installed. Both sections are straight ducts of equal cross-section. The tip of a nozzle-shaped copper block forms the lower wall of the test section and is heated to provide constant wall temperature of $T_w = 373.15\,\mathrm{K}$. For further details we refer to [23].

The simulation domain used for the LES is depicted in figure 1 and consists of two sub-domains, the adiabatic periodic domain D_{per} and the heated test section D_{heat}. The feed line is modelled as a shorter periodic duct piece providing a fully developed turbulent inflow profile for the heated domain as a precursor simulation. The exchange of the outflow, respectively the inflow profile is performed for every time-step. As outflow condition for the heated section we apply a second-order Neumann boundary condition for velocity and density fluctuations and a Dirichlet condition for the pressure. All walls are treated as smooth walls and adiabatic except for the lower wall of D_{heat}, where a spatially and temporally constant temperature of T_w is set. The cross-section of the duct is $L_y \times L_z = 25.8\,\mathrm{mm} \times 6\,\mathrm{mm}$. The resulting

Table 1 Main flow and simulation parameters.

Re_b	Nu	Pr_b	Gr_b	$Re_{\tau,y}$	$Re_{\tau,z}$	T_b [K]	T_w [K]	$L_x \times L_y \times L_z$ [mm^3]
$110 \cdot 10^3$	370.7	3.0	$8.4 \cdot 10^5$	4800	5500	333.15	373.15	$73.0 + 600.0 \times 25.8 \times 6.0$

Table 2 Main parameters for grid shown in figure 2.

	$D_{per}\|_{lower}$	$D_{per}\|_{upper}$	$D_{heat}\|_{lower}$	$D_{heat}\|_{upper}$
$N_x \times N_y \times N_z$	$576 \times 501 \times 141$	$576 \times 501 \times 141$	$4740 \times 501 \times 141$	$4740 \times 501 \times 141$
$\Delta x^+ \times \Delta y^+_{min} \times \Delta z^+_{min}$	$62.7 \times 0.73 \times 1.42$	$62.9 \times 1.24 \times 1.42$	$94.5 \times 1.09 \times 1.42$	$62.8 \times 1.24 \times 1.42$
$\frac{\Delta y_{max}}{\Delta y_{min}} \times \frac{\Delta z_{max}}{\Delta z_{min}}$	33.2×27.3	24.2×27.3	33.2×27.3	24.2×27.3

aspect ratio is $AR = 4.3$ and the hydraulic diameter $d_h = 9.74$ mm. The heated duct is spatially fully represented with the experimental length of $L_{x,heat} = 600$ mm, corresponding to 61.6 d_h. The streamwise length of D_{per} is chosen long enough to resolve all relevant turbulent structures with $L_{x,per} = 7.5 \cdot d_h$. Both domains are simulated simultaneously.

The simulation is conducted in the following way:

- Definition of the velocity distribution for a fully developed laminar duct flow superimposed with white noise of amplitude $A \approx 5\% \, u_b$ on a coarse grid version of D_{per} as initial solution.
- After the initial transition when a fully developed turbulent duct flow is established, interpolation of the velocity field onto the fine grid version of D_{per} and continuation of the simulation for several flow-through times (FTT).
- Use the unheated final flow state of D_{per} as initial condition for the full coupled setup of D_{per} and D_{heat}. The latter is constructed as a sequence of periodic duct sections. Switch on the heating by setting the isothermal wall temperature $T_w = 373.15$ K, respectively $T_w = 393.15$ K.
- Start the coupled simulation for 1.33 FTT with respect to $L_{x,heat}$ and u_b without statistical sampling.
- Start the statistical sampling for the coupled simulation with a constant temporal sampling interval of $\Delta t_{sample} = 0.025 \cdot (d_h/u_b)$ over 20 FTT ($\approx 50 \cdot 10^3$ snapshots) for the case $T_w = 373.15$ K, respectively ≈ 10 FTT ($\approx 24 \cdot 10^3$ snapshots) for the case $T_w = 393.15$ K.

The main flow and simulation parameters are listed in table 1. All Reynolds-numbers are formed using d_h as reference length. The friction Reynolds-numbers are measured in the center of their respective sidewall and represent the adiabatic case. When heating is applied to the lower wall, $Re_{\tau,y}$ increases to 7300. The Prandtl-number is a function of local temperature, the bulk Prandtl-number Pr_b is calculated for the flow state at T_b. The Nusselt-number represents the mean value for the whole domain D_{heat}. The Grashof number describes the ratio of buoyancy to viscous forces. Following [6] buoyancy effects can be neglected when $Gr/Re^2 << 1$. This ratio is $6.9 \cdot 10^{-5}$ in our case, yet we take buoyancy effects into account with the chosen equation system.

Our aim is to perform a well-resolved LES. For this purpose we conducted an extensive grid sensitivity analysis to determine the required grid resolution. This study has been done for the adiabatic duct D_{per}. The resulting grid in the duct cross-section is depicted in figure 2. To reduce numerical costs we apply a 2:1 connection at the interface of boundary layer blocks and the coarser core blocks. To resolve the boundary layer flow the wall-adjacent blocks possess a hyperbolic grid stretching in the respective wall-normal direction. In streamwise direction a uniform discretization is applied for all blocks. For flows with $Pr > 1$ the thermal length scales are smaller than the momentum length scales and the temperature boundary layer is completely contained inside the momentum boundary layer. To sufficiently resolve the wall-normal temperature gradient, the wall-normal resolution at the heatable lower wall is increased. This leads to an asymmetric grid with respect to the $y-$axis. To simplify the exchange of the inflow information between D_{per} and D_{heat} we use a matching interface, hence both domains possess the same cross-section discretization. The main grid parameters for both domains are listed in table 2, separately for the heated lower and the adiabatic upper wall. N_x, N_y and N_z denote the number of cells in each direction. For the discretization of the complete configuration we use in total $\approx 280 \cdot 10^6$ cells. The dimensionless wall distances of the respective wall-adjacent cell are denoted by Δy^+_{min} and Δz^+_{min}, and the constant Δx^+ respectively. They are normalized by the inner length scale $l^+ = \nu_w/u_\tau$ with the friction velocity defined as $u_\tau = \sqrt{\tau_w/\rho_w}$ and τ_w being the wall shear stress. The quantities are evaluated in the center of the respective

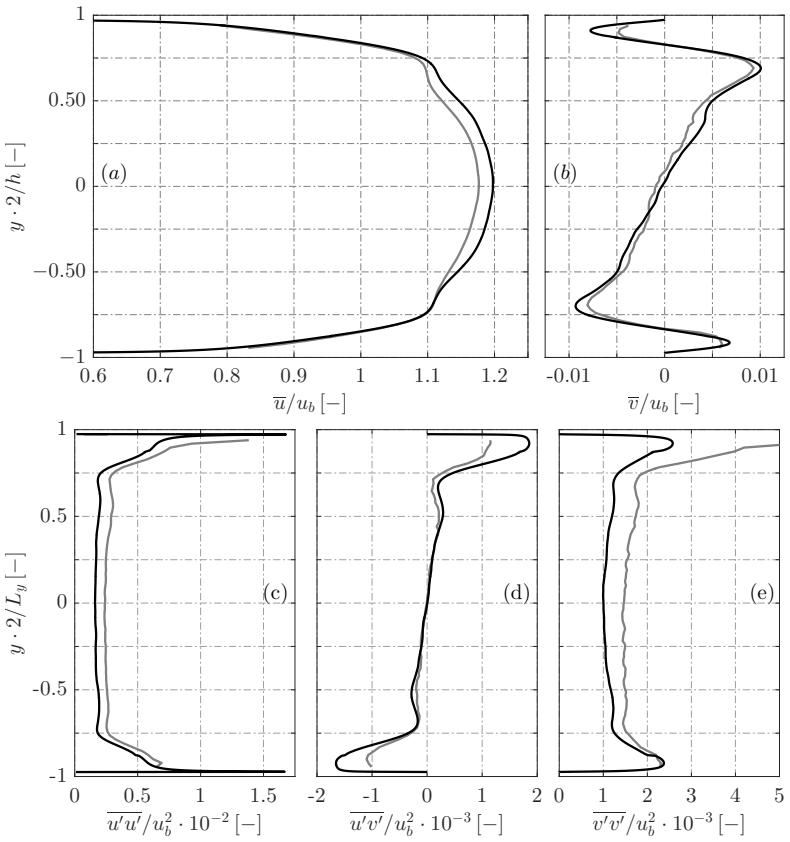

Fig. 3 Comparison of experimental PIV (———) and numerical LES (———) results for the heated duct at T_w = 373.15 K averaged over the experimental field of view. Figures (a)/(b) show the streamwise and heated wall-normal velocity, and figures (c) – (e) the Reynolds stress distribution along the symmetry line z = 0.

wall. The ratios $\frac{\Delta y_{max}}{\Delta y_{min}}$ and $\frac{\Delta z_{max}}{\Delta z_{min}}$ define the coarsening within the boundary layer blocks relating the largest to the smallest cell size.

IV. Results

A. Comparison with reference experiment

The comparison of experimental and numerical results for the case T_w = 373.15 K is shown in figure 3. A similar comparison has already been published in [22]. For both datasets streamwise averaging is performed over the field of view (FOV), which extends from 350 – 400 mm. For the LES data an additional averaging across the symmetry line z = 0 is performed to include the effect of a finite laser sheet thickness of ΔLS = 1 mm. For the latter a constant Gaussian laser intensity distribution is assumed. Fabrication tolerances lead to a slightly narrower duct in the experiment than in the LES. The aspect ratios are $AR_{LES} = 25.8/6.0 = 4.30$ and $AR_{PIV} = 26.1/6.23 = 4.19$. A scaling with respect to the y-axis by the factor (AR_{PIV}/AR_{LES}) is performed for the LES data to account for the difference in the aspect ratio.

The velocity profiles in figure 3 are in good agreement. Until $\approx 2y/L_y = \pm 0.75$ the $\overline{u}$-profiles coincide. The shoulder section close to the lower wall from −0.75 to −0.5 agrees well and close to the upper wall deviations occur due to the slight asymmetry of the experimental data. Due to the narrower cross-section the core velocity in the PIV is slightly smaller than in the LES. The wall-normal velocity shows the secondary flow influence along the duct center line. The $\overline{v}$-profiles also agree well. The positions of the peaks match, however the peak values are higher in the LES. At the upper wall we observe a relatively large deviation for the $\overline{v}$-minimum. We attribute this to the aforementioned asymmetry of the experimental data. Figure 3 (c) – (e) shows the Reynolds stress distributions. The normal stress component $\overline{u'u'}$ shows a satisfactory agreement with the LES. The consistently lower values than in the PIV is probably due to

measurement noise. The $\overline{v'v'}$ profiles coincide in the vicinity of the heated wall, show a similar offset like that in $\overline{u'u'}$ in the center and at the upper wall no comparison is possible due to an overshoot in the experimental data. The shear stress component $\overline{u'v'}$ matches very well except in the vicinity of the walls, where the LES has higher extrema.

The experimental data exhibits uncertainties with respect to laser sheet misalignment and its effective thickness. The latter might be larger than the nominal thickness of $\Delta LS = 1$ mm, which we used for postprocessing the LES results. We investigated the influence on the LES data and observed, that both misalignment and an increased ΔLS would lead to an improved agreement of LES and PIV.

B. The turbulent duct flow flow field

1. The mean heated duct flow field

In the following section, we analyze the turbulent heat transfer problem for the asymmetrically heated high aspect ratio cooling duct based on the numerical LES results. For the two investigated cases the temperature difference between wall and bulk temperature is $\Delta T = 40\,\mathrm{K}$ and $\Delta T = 60\,\mathrm{K}$. The main focus is the investigation of the changes in the turbulent duct flow field along the length of the duct caused by the growth of the temperature boundary layer, respectively the temperature increase and the associated viscosity decrease. Directly at the wall for the case of $T_w = 373.15\,\mathrm{K}$ the kinematic viscosity may drop up to $\nu_w/\nu_b = 0.62$ and for the case of $T_w = 393.15\,\mathrm{K}$ up to $\nu_w/\nu_b = 0.52$ with respect to the bulk temperature value. The viscosity drop over the temperature follows a non-linear function.

The development of the temperature boundary layer along the duct in the vicinity of the heated lower wall is highly affected by the presence of the secondary flow intensifying the mixing of hot and cold fluid. Figure 4 shows the influence of the corner vortices on the temperature distribution at several streamwise locations and the viscosity induced modulation of the secondary flow represented by the vertical velocity component $\overline{v}$. In figure 4 (a) and (h) the vortex system in the lower quarter of the duct is depicted for the adiabatic case. Hence, both pictures are identical. In each duct corner a pair of counter-rotating vortices is forming, a smaller one above the heated wall and a larger one at the lateral sidewall. Focusing now on the left corner, the smaller vortex is a counter-clockwise rotating (CCW) vortex and the larger one is clockwise rotating (CW). For the right corner the rotation direction is mirror-inverted. The influence of each vortex extends to the respective symmetry plane, where it encounters the opposite side vortex. To characterize the strength of the turbulence-induced secondary flow, we introduce the cross-flow velocity magnitude $\overline{u}_{cf} = (\overline{v}^2 + \overline{w}^2)^{0.5}$. The secondary flow is relatively weak, in our case the maximum value of $\overline{u}_{cf}$ is 1.93% of the bulk velocity u_b for the adiabatic duct. This value lies perfectly within the range reported in the literature.

Figure 4 $(b) - (d)$ and $(i) - (k)$ depict the temperature distribution at several streamwise locations along the heated duct. The growth of the temperature boundary layer is determined by heat conduction, turbulent mixing and by secondary flow transport. The strong influence of the latter becomes apparent in the typical bent shape of the temperature distribution. The large vortices convey hot fluid away from the heated wall along the lateral walls into the cooler duct core region. From there they push cold fluid into the respective duct corner approximately along its bisecting line. Along this line the influence regions of large and small vortices of each corner overlap. The small vortices transport heated fluid from the duct corners along the heated wall into its centre and then upwards. The mixing motion increases the overall heat transfer. Furthermore, it creates a non-uniform heat flux in spanwise direction. In the duct corner the temperature gradient with respect to T_w is increased by the secondary flow leading to a higher heat flux than in the wall centre, where the small vortices decrease the temperature gradient. In total the temperature increase is relatively moderate and restricted to the lower quarter of the duct. The theoretically possible maximum temperature increase $\Delta T_{max} = T_b - T_w$ is reached only directly at the heated wall and quickly drops in wall-normal direction. In the duct end section at 600 mm, $z = 0$ and $2y/L_y = -0.975$, $\Delta T \approx 12.7\,\mathrm{K}$ for the case $T_w = 373.15\,\mathrm{K}$ and $\Delta T \approx 19.9\,\mathrm{K}$ for the case $T_w = 393.15\,\mathrm{K}$. At $z = 0$ and $2y/L_y = -0.5$ ΔT has dropped to $\approx 0.74\,\mathrm{K}$ for the low T_w case and to $\approx 1.0\,\mathrm{K}$ for the high T_w case. The latter two values underline the significant impact of the secondary flow on heat transfer mixing hot and cold fluid over large distances.

The temperature increase is accompanied by a viscosity decrease, which affects the strength of the secondary flow. Figures 4 $(e) - (g)$ and $(l) - (m)$ depict the distribution of the heated wall-normal velocity and its change with respect to the adiabatic case along the duct length. Even though the temperature increase is relatively moderate, we observe a significant weakening of the secondary flow strength, especially visible for the larger vortex along the lateral wall. For $T_w = 373.15\,\mathrm{K}$ the upwards motion, for example at $(2y/L_y, 2z/L_z) = (-0.75, 0.95)$ is reduced by $(\overline{v} - \overline{v}_{per})/\overline{v}_{per} = -17.02\%$ and for $T_w = 393.15\,\mathrm{K}$ by -21.88%. The upwards motion of the small vortex is also reduced, for example at $(2y/L_y, 2z/L_z) = (-0.95, 0.0)$ by -19.44% for the lower and by -8.33% for the higher wall

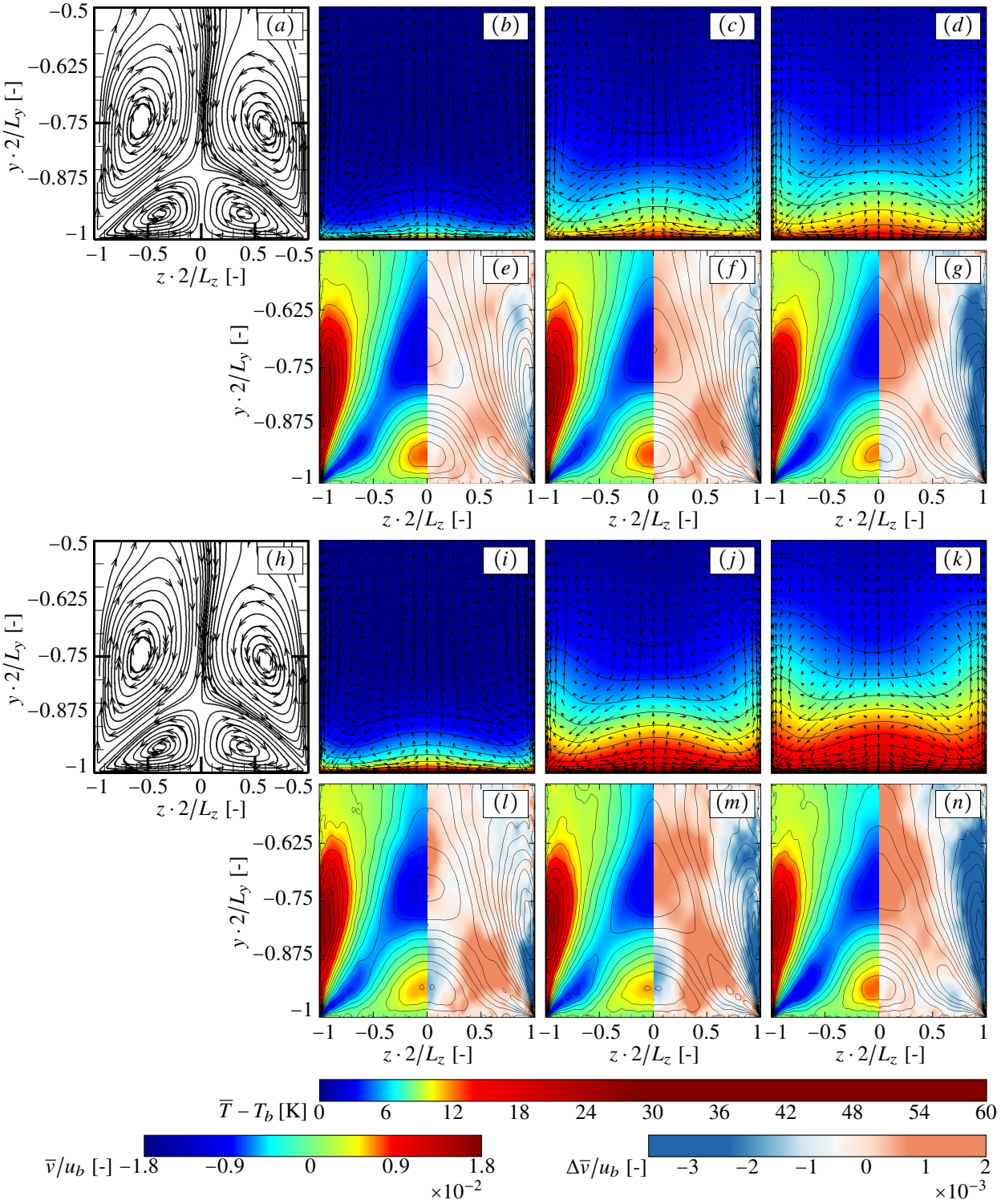

Fig. 4 Development of the temperature boundary layer and the accompanying change in the secondary flow represented by the heatable wall-normal velocity $\overline{v}$. On the top half the case $T_w = 373.15\,\mathrm{K}$ and on the bottom half the case $T_w = 393.15\,\mathrm{K}$ is depicted. The evaluation is done for the lower quarter of the duct at different streamwise positions of $100\,\mathrm{mm}$ for the left column, $400\,\mathrm{mm}$ for the middle column and $600\,\mathrm{mm}$ for the right column. Figures (a) and (h) show the vortex system for the adiabatic duct. The temperature increase is shown in the respective first row and the secondary flow velocity in the second. For the latter, the left half of each picture contains $\overline{v}$ and the right half the change of $\overline{v}$ with respect to the adiabatic case, $\Delta\overline{v} = \overline{v} - \overline{v}_{per}$.

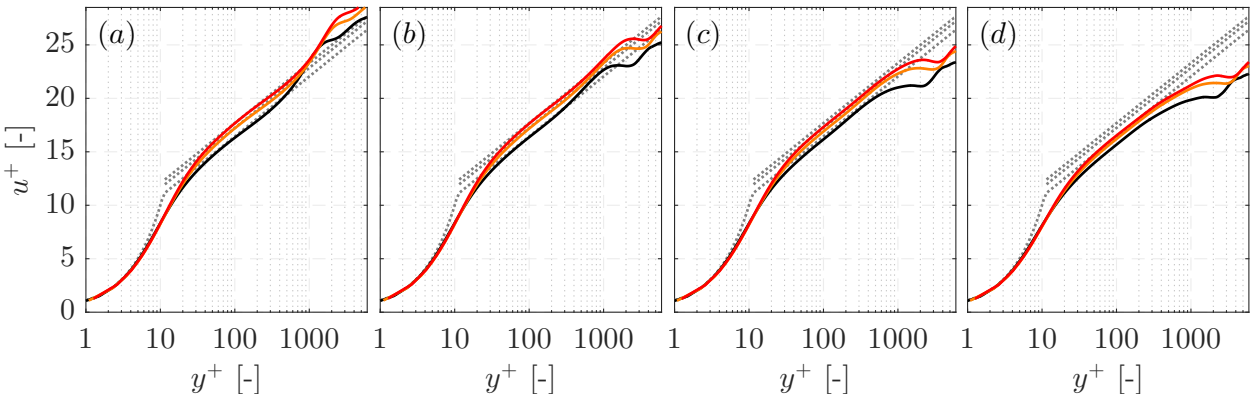

Fig. 5 Profiles of mean streamwise velocity along the y-axis at (from left to right) $2z/L_z = 0.0$, $2z/L_z = 1/2$, $2z/L_z = 3/4$ and $2z/L_z = 5/6$ for the adiabatic (———), the heated duct at $T_w = 373.15$ K (———) and the heated duct at $T_w = 393.15$ K (———). The law of the wall is represented by (·····).

temperature case. Comparing figures 4 (e) – (g) individually with (l) – (m) it becomes apparent, that the higher wall temperature, respectively the higher viscosity reduction, leads to a stronger reduction of the secondary flow strength in streamwise direction.

As the secondary flow is turbulence-induced, we further analyze the influence of the asymmetric wall heating on the lower wall boundary layer. Figure 5 shows the effect of the temperature increase on the boundary layer velocity profile at several spanwise locations comparing the adiabatic with both heated cases. For all three datasets a streamwise averaging is performed, for the adiabatic case over $L_{x,per} = 7.5\,d_h$ and for the heated cases over the last $7.5\,d_h$ of D_{heat}. The boundary layer velocity profile can be described by the law of the wall, $u^+ = y^+$ in the viscous sublayer and $u^+ = 1/\kappa \cdot \ln y^+ + B$ in the log-layer region. For the wall center in figure 5 (a), we observe that the viscosity decrease leads to an upwards shift in the log-law region, whereas the viscous sublayer of the velocity profile remains unaffected. For the lower wall temperature case the integration constant B increases from 5.2 to 6.0 and for the high wall temperature case to 6.45. The velocity profile slope and hence the von Kármán constant remain constant at $\kappa = 0.41$. These results are in good agreement with [24]. For the off-center locations figure 5 (b) – (d) we observe the same trend. Additionally, in figure 5 (c) and stronger in (d) the influence of the lateral wall becomes apparent leading to a downwards shift of the velocity profiles. Figure 6 depicts the heating induced changes in the Reynolds stresses at the same spanwise locations as before. The $\overline{u'u'}$-peak is shifted closer to the wall, while the maximum value remains approximately constant. Counterintuitively, all turbulence intensities are reduced within the whole boundary layer when heating is applied. However, following [24] and [25] the temperature increase, respectively the viscosity decrease, has a stabilizing effect on the turbulent boundary layer reducing the turbulence intensities. As before, in figures 6 (c) and (d) the influence of the lateral wall is apparent leading for example to an increase of the $\overline{u'u'}$-profile along the y-axis after its minimum at $2y/L_y \approx -0.975$.

2. The mean streamwise vorticity distribution

In this section we investigate the influence of asymmetrical wall-heating on the secondary flow by analyzing the development of the mean streamwise vorticity $\overline{\omega}_x$ and the single terms of the streamwise vorticity equation 1 along the duct length.

Figure 7 presents the mean streamwise vorticity distribution and the corner vortices visualized by streamlines for the lower duct half of the adiabatic case and the $T_w = 373.15$ K case at 595 mm. The respective zoom into the duct corner is given in figures 8 (a) and (d). Focusing on figure 7 (a) on the $z < 0$ half, a primary negative vorticity region is located in the small vortex area and an associated layer of opposite sign directly at the heatable wall, see figure 8 (a) for a detailed view. As [14] showed, this associated layer becomes narrower with increasing Reynolds number. A primary positive vorticity region is located in the large vortex area near the lateral wall, again accompanied by a layer of negative vorticity directly at the wall. The vorticity distribution is highly asymmetric due to the high aspect ratio duct geometry. The primary negative $\overline{\omega}_x$ region is compressed, whereas the primary positive $\overline{\omega}_x$ region is stretched compared to a square duct. [14] divides the cross-section vorticity in two contributions, the core vorticity and the

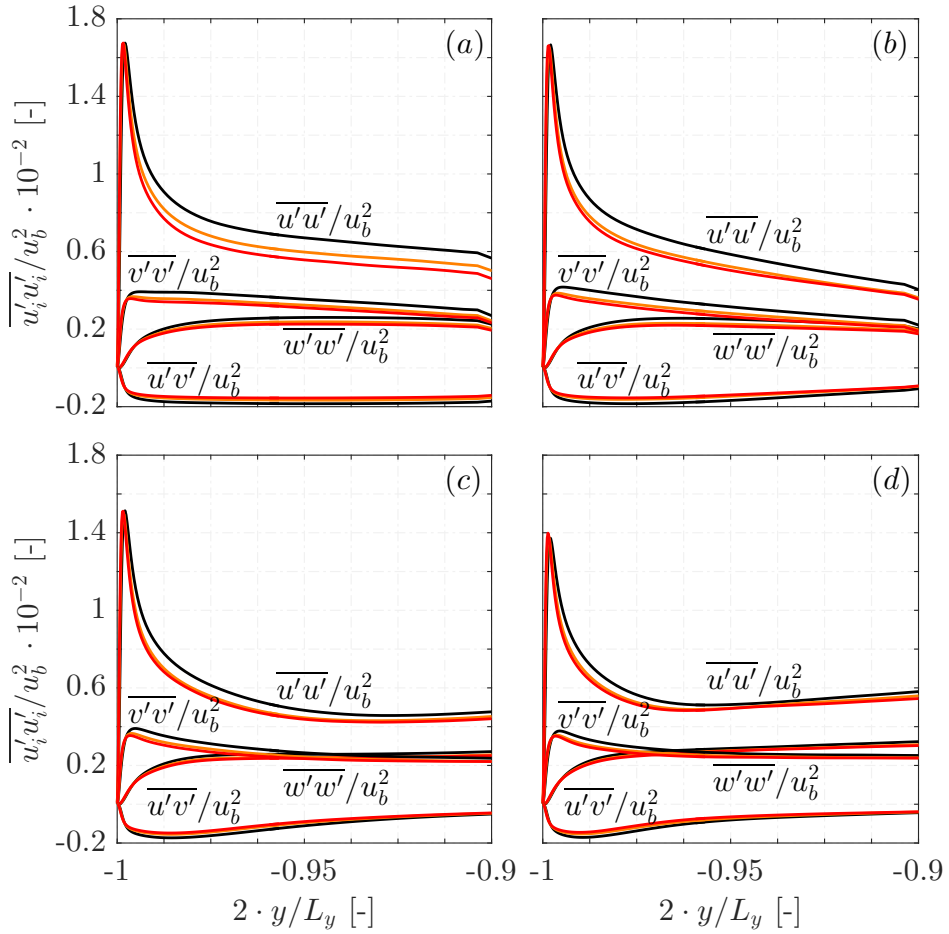

Fig. 6 Profiles of Reynolds stresses along the y-axis at (from left to right) $2z/L_z = 0.0$, $2z/L_z = 1/2$, $2z/L_z = 3/4$ and $2z/L_z = 5/6$ for the adiabatic (———), the heated duct at $T_w = 373.15$ K (———) and the heated duct at $T_w = 393.15$ K (———).

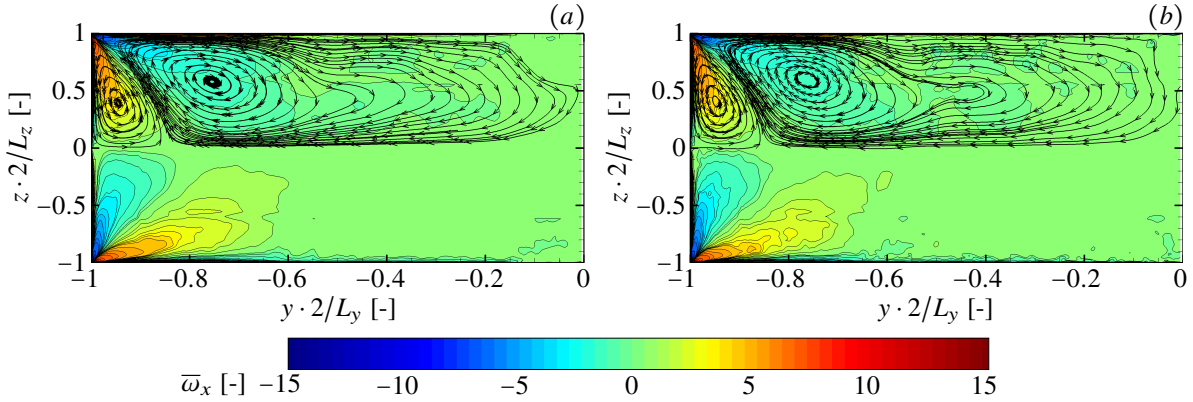

Fig. 7 Mean streamwise vorticity $\overline{\omega}_x$ and streamlines in the lower duct half for (a) the adiabatic case and (b) the $T_w = 373.15$ K case in the end section at $x = 595$ mm, $\overline{\omega}_x$ is normalized by (u_b/d_h). For (a) streamwise averaging is performed over $7.5\,d_h$ and for (b) over 10 mm. For both the duct symmetry is utilized.

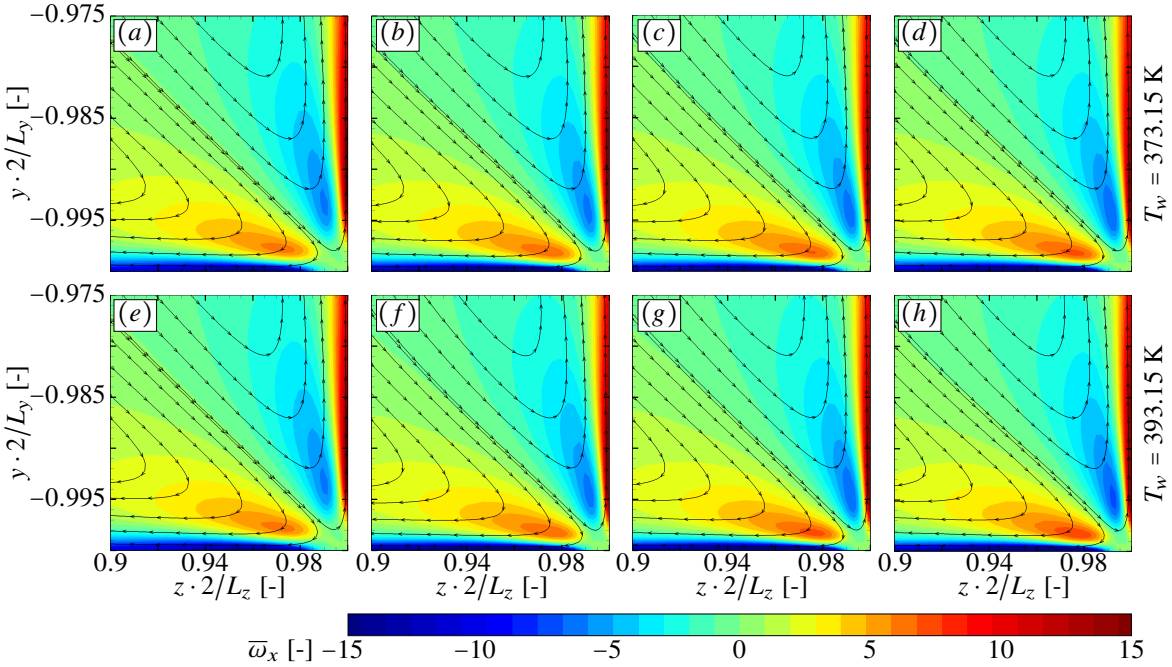

Fig. 8 Mean streamwise vorticity $\overline{\omega}_x$ and streamlines in the lower right duct corner for the adiabatic duct (left column) and at streamwise positions (from left to right) of 50 mm, 200 mm and 595 mm. The top row contains the results for the lower wall temperature and the bottom row for the higher wall temperature. $\overline{\omega}_x$ is normalized by (u_b/d_h). Streamwise averaging is performed over 7.5 d_h for the adiabatic and over 10 mm for the heated duct, and the duct symmetry is utilized.

corner vorticity. The latter comprises the strongest vorticity in the flow field, which is located at the corner bisectors and at the walls. However, in comparison to the weaker core vorticity its contribution to the secondary flow motion is less important. The core vorticity scales in outer units as (u_b/d_h) and for the corner vorticity [14] proposed a mixed scaling of inner and outer units as (u_b/l^+) with l^+ being the viscous length scale. Hence, the contribution of the corner vorticity to the total circulation decreases with increasing Re, respectively Re_τ. For our study we use the term (u_b/d_h) for non-dimensionalization of the streamwise vorticity in the whole cross-section to clarify the effect of wall-heating on the vorticity distribution. The comparison of figures 7 (a) and (b) shows that the positive vorticity area becomes slightly weaker, which is in agreement with the reduced secondary flow velocity results presented in the previous section. Note, figure 7 (a) is slightly smoother as (b) as the streamwise averaging is performed over 7.5 d_h for the former and over 10 mm for the latter.

Figure 8 presents the influence of the wall-heating on the corner vorticity distribution. For the T_w = 373.15 K case, we observe first, that the vorticity peaks move slightly closer towards the duct corner, compare figures 8 (a) and (b). Second, from (a) to (d) the vorticity amplitude for both the peaks located around the corner bisector as well as the wall layers increases. This is in accordance with [14], who found that the streamlines penetrate deeper into the duct corners with increasing Reynolds numbers leading to a higher vorticity. In our case the local Re and Re_τ increases due to the asymmetric heating and the associated viscosity decrease. Comparing the top row results for the lower wall temperature case with the bottom row results this effect becomes stronger.

In figures 9, 10 and 11 the single terms of the streamwise vorticity equation $T_{\overline{\omega}_x,conv}$, $T_{\overline{\omega}_x,visc}$ and $T_{\overline{\omega}_x,turb}$ are shown, see equation 1. The two turbulence terms are merged together. Normalization is done by $(u_b/d_h)^2$, the assumed scaling of the $\overline{\omega}_x$ time derivative. The sign of $T_{\overline{\omega}_x,conv}$ corresponds to the notation in equation 1, the term being on the left hand side. Along the duct length, from figures 9 (a) to (d), $T_{\overline{\omega}_x,conv}$ follows a similar trend as $\overline{\omega}_x$. The peaks move towards the duct corner, compare especially figure 9 (a) and (b), and the peak amplitudes increase steadily. No qualitative difference is found between the two wall temperature cases. Compared to the other two terms $T_{\overline{\omega}_x,conv}$ is the weakest. This result supports [2] and [14], who concludes that convection plays not an important role for streamwise vorticity dynamics.

The viscous term $T_{\overline{\omega}_x,visc}$ reaches very high values close to the walls and is negligible elsewhere. The lens-shaped

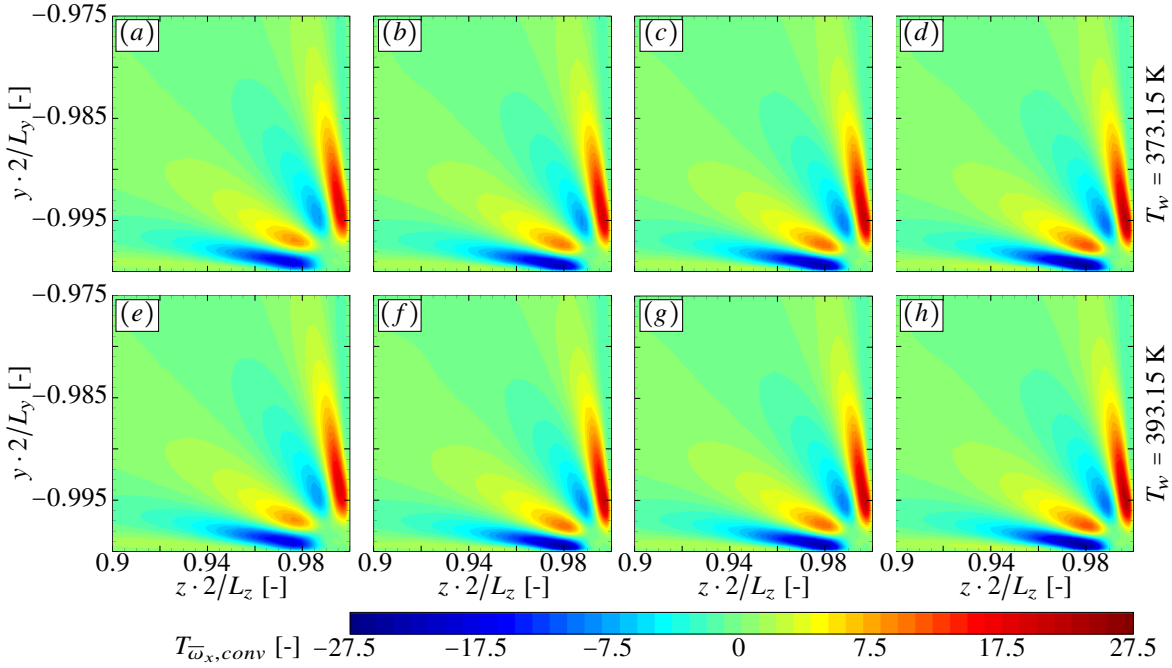

Fig. 9 Convective mean streamwise vorticity term $T_{\overline{\omega}_x,conv}$ for the adiabatic duct (left column) and at streamwise positions (from left to right) of 50 mm, 200 mm and 595 mm. The top row contains the results for the lower wall temperature and the bottom row for the higher wall temperature. $T_{\overline{\omega}_x,conv}$ is normalized by $(u_b/d_h)^2$. Streamwise averaging is performed over $7.5\,d_h$ for the adiabatic and over 10 mm for the heated duct, and the duct symmetry is utilized.

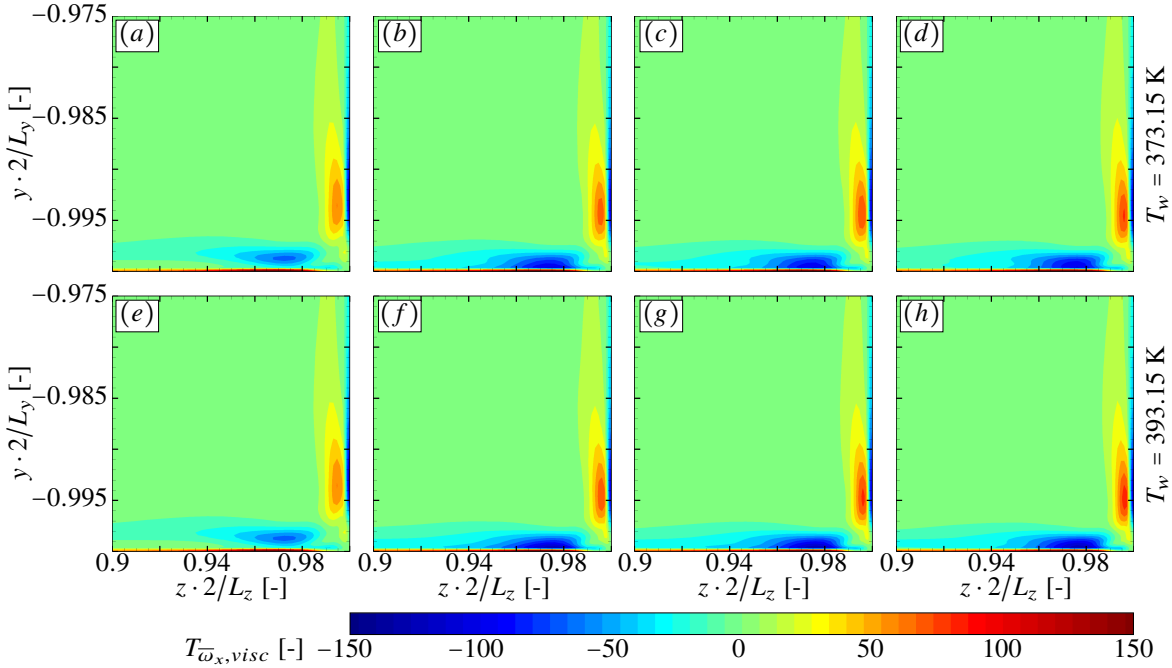

Fig. 10 Viscous mean streamwise vorticity term $T_{\overline{\omega}_x,visc}$ for the adiabatic duct (left column) and at streamwise positions (from left to right) of 50 mm, 200 mm and 595 mm. The top row contains the results for the lower wall temperature and the bottom row for the higher wall temperature. $T_{\overline{\omega}_x,visc}$ is normalized by $(u_b/d_h)^2$. Streamwise averaging is performed over $7.5\,d_h$ for the adiabatic and over 10 mm for the heated duct, and the duct symmetry is utilized.

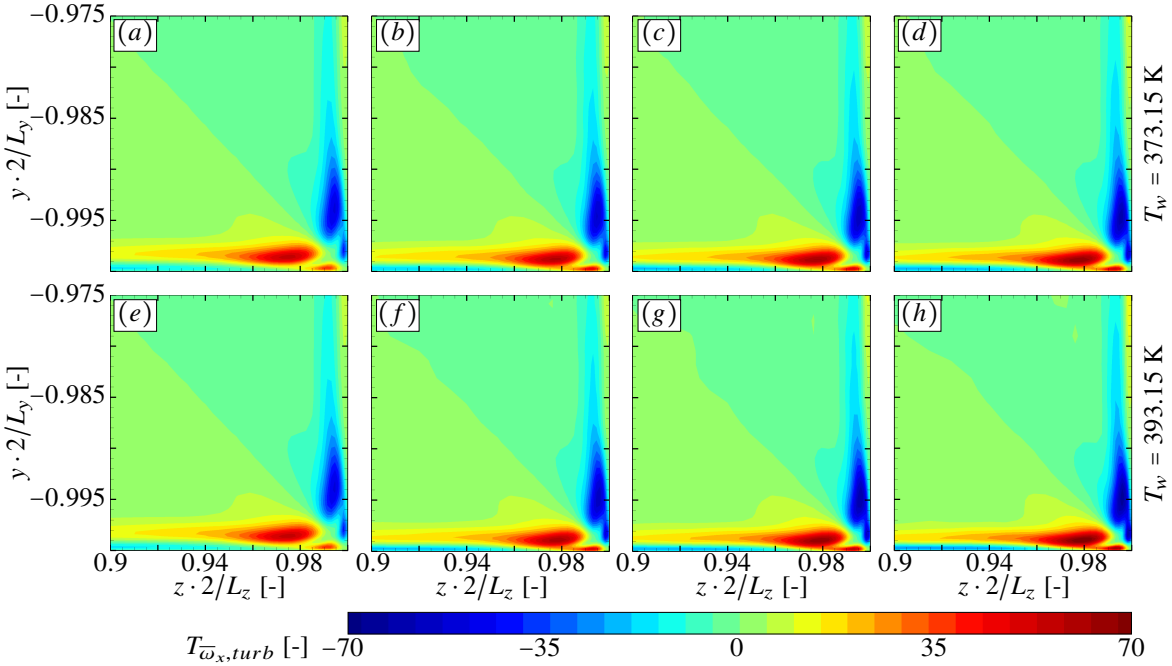

Fig. 11 Turbulence mean streamwise vorticity term $T_{\overline{\omega}_x,turb}$ for the adiabatic duct (left column) and at streamwise positions (from left to right) of 50 mm, 200 mm and 595 mm. The top row contains the results for the lower wall temperature and the bottom row for the higher wall temperature. $T_{\overline{\omega}_x,turb}$ is normalized by $(u_b/d_h)^2$. Streamwise averaging is performed over 7.5 d_h for the adiabatic and over 10 mm for the heated duct, and the duct symmetry is utilized.

areas of negative values at the heatable wall, respectively of positive values at the lateral wall, are accompanied by a small layer of opposite sign directly at the respective wall. When heating is applied at the lower wall both lens-shaped peaks wander towards the corner and towards their respective wall. The negative value peak moves much closer to the wall, so that its shape changes and its area is enlarged. Along the duct length the peak amplitudes increase. For the higher wall temperature case the effects become again more prominent. The turbulence term $T_{\overline{\omega}_x,turb}$ comprising the Reynolds shear stress term and the Reynolds normal stress difference term is understood as production term for the streamwise vorticity, see equation 1. The cross-section distribution consists of two lens-shaped positive peaks at the heatable wall, one larger and a smaller one in the duct corner and the same two structures with opposite sign mirrored at the corner bisecting line. In streamwise direction the larger peaks move closer to the corner, whereas the smaller peaks remain at their position, compare figures 11 (a) and (b). From (a) to (d) the peak amplitudes of both larger and smaller peaks steadily increase and the peaks grow together. Comparing the top row results with those in the bottom row, this effect again becomes more prominent.

3. The turbulent Prandtl number distribution

In the following section we investigate the cross-section turbulent Prandtl number Pr_t distribution for the heated duct. The turbulent Prandtl number is defined as the ratio of turbulent eddy viscosity ν_t and turbulent eddy thermal diffusivity α_t. For Pr_t the Reynolds analogy assuming an equal turbulent heat flux and momentum flux is often utilized yielding a constant value of $Pr_t = 1$. As Pr_t strongly depends on the molecular Prandtl number a prevalent approach is also to set Pr_t to a fix value based on experimental data. An extensive overview is given by [26].

As already mentioned $Pr_t = \nu_t/\alpha_t$. For a heated turbulent boundary layer (TBL) with the x-axis marking the streamwise and the y-axis marking the wall-normal direction, the eddy viscosity and diffusivity are defined as

$$\overline{u'v'} = -\nu_t \cdot \frac{\partial \overline{u}}{\partial y}, \quad \overline{T'v'} = -\alpha_t \cdot \frac{\partial \overline{T}}{\partial y}. \tag{2}$$

The TBL-definition has also been applied for more complex flow configurations for example by [27] for a numerical

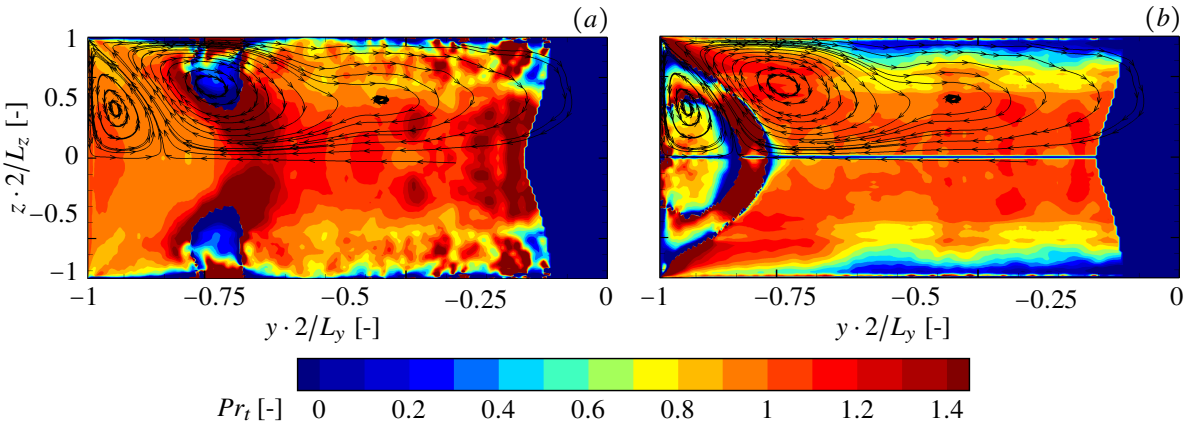

Fig. 12 Turbulent Prandtl number Pr_t distribution in the lower half of the duct cross-section at a streamwise location of 595 mm calculated following the standard TBL definition for (a) the y-direction and (b) the z-direction for the case with $T_w = 373.15$. Streamwise averaging is performed over 10 mm and the duct symmetry is utilized. Pr_t is calculated where the fluid temperature is $\overline{T} - T_b > 0.05$ K.

investigation of a mixed convection configuration consisting of a channel with one heated and one adiabatic wall and a heated cylinder slightly above the heated wall. [28] used this definition for an experimental investigation of a square duct flow with all four walls being heated. Figure 12 depicts the turbulent Prandtl number distribution defined following the TBL-definition for the (a) y-direction and for the (b) z-definition to also account for the lateral sidewalls in the end cross-section at $x = 595$ mm. We observe, that due the presence of the secondary flow the TBL-definition cannot be used to derive the Pr_t-distribution in the duct cross-section. In regions mainly affected by the large vortices especially the Pr_t-definition following the y-TBL formulation fails, whereas the results in the vicinity of the heated walls seem reasonable. For the the Pr_t-definition following the z-TBL formulation the results in regions mainly affected by the small vortices are incorrect, whereas the results in the rest of the cross-section seem reasonable. For the evaluation of the cross-section turbulent Prandtl number we reformulate equation 2 to take the influence of both sidewall boundary layers into account at every point of the cross-section flow field. We define the vectors

$$\mathbf{v}_{1\nu} = \begin{bmatrix} \overline{u'v'} \\ \overline{u'w'} \end{bmatrix}, \quad \mathbf{v}_{2\nu} = -\begin{bmatrix} \partial\overline{u}/\partial y \\ \partial\overline{u}/\partial z \end{bmatrix}, \quad \mathbf{v}_{1\alpha} = \begin{bmatrix} \overline{T'v'} \\ \overline{T'w'} \end{bmatrix}, \quad \mathbf{v}_{2\alpha} = -\begin{bmatrix} \partial\overline{T}/\partial y \\ \partial\overline{T}/\partial z \end{bmatrix}. \tag{3}$$

Using the least square optimization method to calculate the eddy viscosity the term $(\nu_t \cdot \mathbf{v}_{2\nu} - \mathbf{v}_{1\nu})^2$ has to be minimized for every point in the cross-section and likewise $(\alpha_t \cdot \mathbf{v}_{2\alpha} - \mathbf{v}_{1\alpha})^2$ for the eddy diffusivity. The eddy viscosity and diffusivity are then calculated as

$$\nu_t = \frac{\mathbf{v}_{1\nu} \cdot \mathbf{v}_{2\nu}}{|\mathbf{v}_{2\nu}|^2}, \quad \alpha_t = \frac{\mathbf{v}_{1\alpha} \cdot \mathbf{v}_{2\alpha}}{|\mathbf{v}_{2\alpha}|^2}. \tag{4}$$

The resulting Pr_t-distribution for both wall temperature cases at several streamwise locations along the heated duct are depicted in figure 13. For each picture a streamwise averaging is performed over the interval from 5 mm left to 5 mm right of the respective x-position. Additionally the duct symmetry is utilized by averaging the $z < 0$ and the $z > 0$ quadrant. The turbulent Prandtl number is evaluated when the local heating $\overline{T} - T_b$ surpasses a threshold of 0.05 K and set to zero otherwise. With increasing streamwise distance the thus defined evaluation boundary is moving from the heated wall into the core due to the mixing of hot and cold fluid by the secondary flow. Overall, the Pr_t-distribution following equation 4 is reasonable and the distorted regions visible in figure 12 using the TBL-formulation following equation 2 have vanished. The range of the turbulent Prandtl number distribution is qualitatively in good agreement with data available in the literature, for example with the study by [27] using also liquid water, however, at a lower temperature of $T_b = 284$ K and $T_w = 318$ K.

For the description of the cross-section Pr_t-distribution we now focus on figure 13 (g). The turbulent Prandtl number directly at the wall in its center $z = 0$ starts with a value of 0.94. Directly above the heated wall, in the region

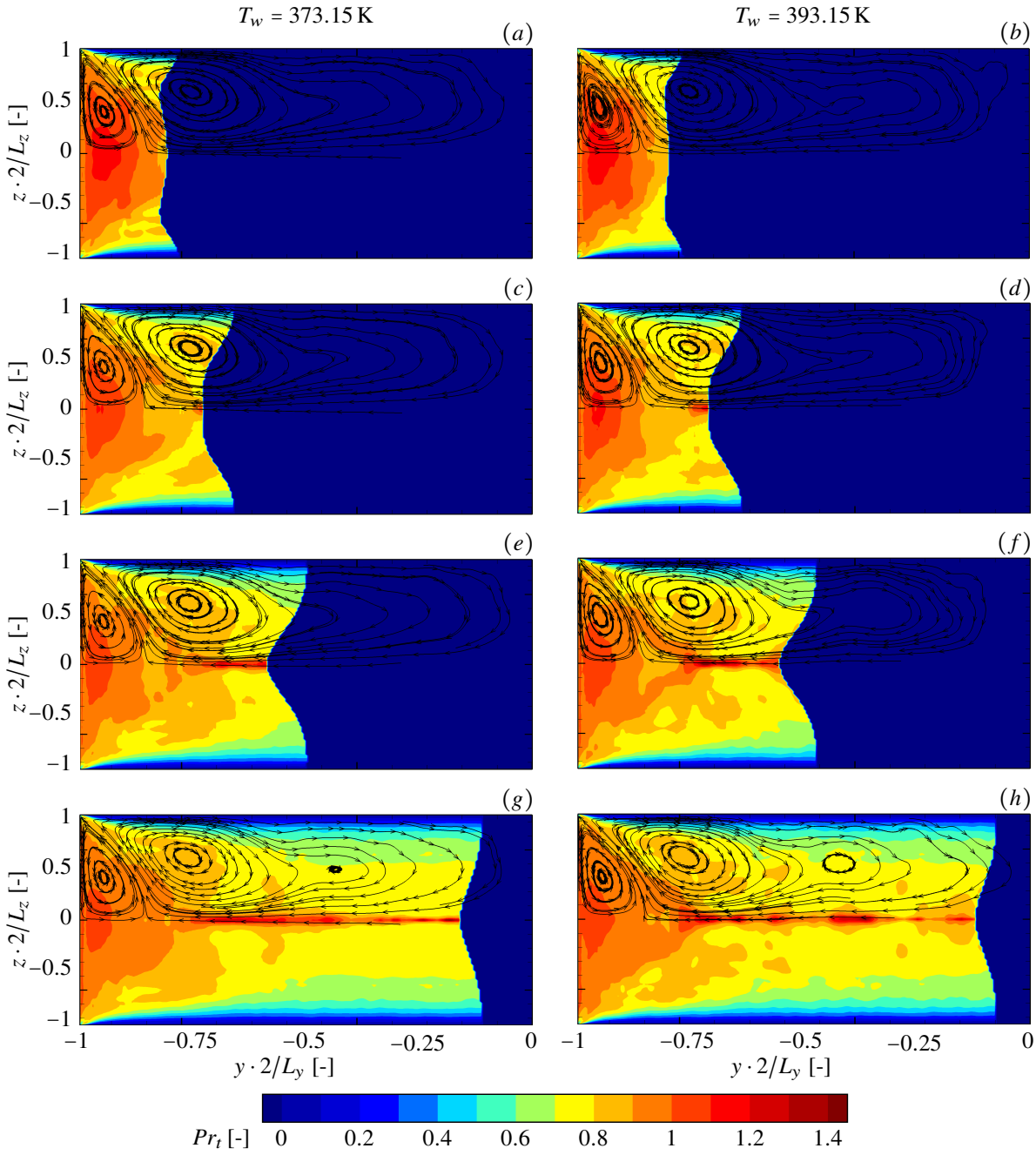

Fig. 13 Turbulent Prandtl number Pr_t distribution in the lower half of the duct cross-section at streamwise locations of 50 mm, 100 mm, 200 mm and 595 mm (from top to bottom). Streamwise averaging is performed over 10 mm for each position and the duct symmetry is utilized. On the left, the case with T_w = 373.15 and on the right the case with T_w = 393.15 is shown. Pr_t is calculated where the fluid temperature is $\overline{T} - T_b > 0.05$ K.

affected by the small corner vortices a dome-shaped region of increased turbulent Prandtl number is present. The observed increase is a direct consequence of the mixing motion of the secondary flow as the location and shape of the region matches perfectly to the secondary flow structure. The maximum value of $Pr_t = 1.06$ is reached in the center, where the interaction of both small vortices leads to a strong upwards flow. In the outer regions of the dome-shaped area, where the small vortices interact with their respective large vortex Pr_t drops to values between ≈ 0.9 and ≈ 0.95. At $2z/L_z \approx -0.7$ a narrow maximum of $Pr_t \approx 1.3$ located along the center line is reached. This maximum is caused by the strong downwards motion of the large vortices. At the lateral sidewalls Pr_t equals almost zero as the eddy diffusivity is two orders of magnitude larger than the eddy viscosity. This is a consequence of the adiabatic wall boundary condition. At $2y/L_y \approx -0.7$ and above, Pr_t increases in lateral wall-normal direction until the narrow maximum in the center. Like the small vortices also the large vortices increase the turbulent Prandtl number. However, due to the proximity of the adiabatic walls the effect is not as strong as for the dome-shaped area. In the vortex core of the large vortices $Pr_t \approx 0.825$, whereas in the vortex core of the small vortices $Pr_t \approx 0.95$.

In streamwise direction, i.e. from figures 13 (a) over (c) and (e) to (g), we observe that the dome-shaped area of increased turbulent Prandtl number gets weaker, the maximum value in the center drops from 1.16 at 50 mm over 1.11 and 1.08 to 1.06 at 595 mm. Between the two cases of $T_w = 373.15\,\mathrm{K}$ and $T_w = 393.15\,\mathrm{K}$ no qualitative difference in the cross-sections is visible. Note, the results of the lower wall temperature case are slightly smoother due to the longer averaging time. Based on the turbulent Prandtl number distributions we come to the conclusion, that the assumption of a constant value for Pr_t is invalid for turbulent heat transfer in an asymmetrically heated high aspect ratio duct due to the strong influence of the secondary flow affecting the cross-section turbulence distribution as well as velocity and temperature gradients and eventually the turbulent Prandtl number.

V. Summary and Conclusion

We investigated the three-dimensional turbulent flow field of a straight high aspect ratio cooling duct operated with liquid water at a Reynolds-number of $110 \cdot 10^3$ with asymmetric wall heating using a well-resolved LES. Three configurations have been considered for the analysis, an adiabatic duct flow and a duct flow with one of the short sidewalls being heated with $\Delta T = T_w - T_b = 40\,\mathrm{K}$ and $\Delta T = 60\,\mathrm{K}$. For the $\Delta T = 40\,\mathrm{K}$ case good agreement with experimental PIV measurements by [23] for the same configuration has been achieved for mean velocity and Reynolds stresses.

We analyzed the spatial development of the temperature boundary layer along the duct and the influence of the turbulence-induced secondary flow on its shape. The secondary is characterized by a pair of counter-rotating vortices forming in each duct corner. Their strength is relatively weak, in our case the maximum cross-flow velocity is $\approx 2\%$ of the bulk velocity. However, the strong impact on the temperature distribution is clearly visible. The temperature increase leads to a significant viscosity drop in the vicinity of the heated wall. We observed a significant weakening of the secondary flow strength in streamwise direction, especially for the large vortex. As the secondary flow is turbulence-induced, we further investigated the effects of the viscosity drop on the near wall turbulence and velocity at several spanwise positions. In agreement with previous studies by [25] and [24], we observed a constant upwards shift of the boundary layer velocity profile and a reduction of turbulence intensity in all directions. The effects became more prominent in the high wall temperature case.

Furthermore we investigated the streamwise vorticity distribution and its dynamics with a focus on the duct corner region. We observed, that with heating applied to the lower wall, the streamlines penetrate deeper into the duct corner and the peak amplitudes steadily increase. Evaluating the single terms in the vorticity equation we found, that the convection term is far weaker than the viscous diffusion and the turbulence term. Hence the vorticity dynamics are mainly determined by the balance of the latter two terms. Our observations support recent DNS results by [14] for an adiabatic square duct. For the investigation of the turbulent Prandtl number distribution we showed that for our case the standard turbulent boundary layer definition of Pr_t is insufficient. We hence introduced a new formulation taking the additional lateral walls into account. We concluded that the prevalent assumption of a constant value for Pr_t is invalid for turbulent heat transfer in an asymmetrically heated high aspect ratio duct due to the strong secondary flow influence on the cross-section distributions of turbulence as well as velocity and temperature gradients and eventually the turbulent Prandtl number.

VI. Acknowledgement

Financial support has been provided by the German Research Foundation (Deutsche Forschungsgemeinschaft – DFG) within the framework of the Sonderforschungsbereich Transregio 40, SFB-TRR40 (Technological foundations for the design of thermally and mechanically highly loaded components of future space transportation systems). Computational resources have been provided by the Leibniz Supercomputing Centre Munich (LRZ).
The authors acknowledge helpful discussions with the people from the Institute of Fluid Mechanics, Technische Universität Braunschweig, who conduct the experimental investigation of the reference case; namely Peter Scholz, Henrik Rochlitz and Oliver Günther.

References

[1] Demuren, A. O., and Rodi, W., "Calculation of turbulence-driven secondary motion in non-circular dcuts," *Journal of Fluid Mechanics*, Vol. 140, 1984, pp. 189–222.

[2] Gavrilakis, S., "Numerical simulation of low-Reynolds-number turbulent flow through a straight square duct," *Journal of Fluid Mechanics*, Vol. 244, 1992, pp. 101–129.

[3] Baines, W. D., and Brundrett, E., "The production and diffusion of vorticity in duct flow," *Journal of Fluid Mechanics*, Vol. 19, 1964, pp. 375–394.

[4] Gessner, F. B., and Jones, J. B., "On some aspects of fully-developed turbulent flow in rectangular channels," *Journal of Fluid Mechanics*, Vol. 23, No. 4, 1965, pp. 689–713.

[5] Launder, B. E., and Ying, W. M., "Secondary flows in ducts of square cross-section," *Journal of Fluid Mechanics*, Vol. 54, No. 2, 1972, pp. 289–295.

[6] Wardana, I. N. G., Ueda, T., and Mizomoto, M., "Effect of strong wall heating on turbulence statistics of a channel flow," *Experiments in Fluids*, Vol. 18, No. 1, 1994, pp. 87–94.

[7] Monty, J. P., "Developments In Smooth Wall Turbulent Duct Flows," Ph.D. thesis, The University of Melbourne, 2005.

[8] Madabhushi, R. K., and Vanka, S. P., "Large eddy simulation of turbulence-driven secondary flow in a square duct," *Physics of Fluids A: Fluid Dynamics*, Vol. 3, No. 11, 1991, pp. 2734–2745.

[9] Huser, A., and Biringen, S., "Direct numerical simulation of turbulent flow in a square duct," *Journal of Fluid Mechanics*, Vol. 257, 1993, pp. 65–95.

[10] Salinas-Vásquez, M., and Métais, O., "Large-eddy simulation of the turbulent flow through a heated square duct," *Journal of Fluid Mechanics*, Vol. 453, 2002, pp. 201–238.

[11] Hébrard, J., Salinas-Vásquez, M., and Métais, O., "Spatial development of turbulent flow within a heated duct," *Journal of Turbulence*, Vol. 6, No. 8, 2005.

[12] Sekimoto, A., Kawahara, G., Sekiyama, K., Uhlmann, M., and Pinelli, A., "Turbulence- and buoyancy-driven secondary flows in a horizontal square duct heated from below," *Physics of Fluids*, Vol. 23, No. 7, 2011, p. 075103.

[13] Zhu, Z., Yang, H., and Chen, T., "Numerical study of turbulent heat and fluid flow in a straight square duct at higher Reynolds numbers," *International Journal of Heat and Mass Transfer*, Vol. 53, No. 1-3, 2010, pp. 356–364.

[14] Pirozzoli, S., Modesti, D., Orlandi, P., and Grasso, F., "Turbulence and secondary motions in square duct flow," *Journal of Fluid Mechanics*, Vol. 840, 2018, pp. 631–655.

[15] Choi, H. S., and Park, T. S., "The influence of streamwise vortices on turbulent heat transfer in rectangular ducts with various aspect ratios," *International Journal of Heat and Fluid Flow*, Vol. 40, 2013, pp. 1–14.

[16] Vinuesa, R., Noorani, A., Lozano-Duran, A., El Khoury, G., Schlatter, P., Fischer, P. F., and Nagib, N. M., "Aspect ratio effects in turbulent duct flows studied through direct numerical simulation," *Journal of Turbulence*, Vol. 15, No. 10, 2014, pp. 677–706.

[17] IAPWS, "Release on the IAPWS Formulation 2008 for the Viscosity of Ordinary Water Substance," Available from http://www.iapws.org, 2008.

[18] IAPWS, "Release on the IAPWS Formulation 2011 for the Thermal Conductivity of Ordinary Water Substance," Available from http://www.iapws.org, 2011.

[19] Hickel, S., Adams, N. A., and Domaradzki, J. A., "An adaptive local deconvolution method for implicit LES," *Journal of Computational Physics*, Vol. 213, No. 1, 2006, pp. 413–436.

[20] Hickel, S., Egerer, P., C, and Larsson, J., "Subgrid-scale modeling for implicit large eddy simulation of compressible flows and shock-turbulence interaction," *Physics of Fluids*, Vol. 26, No. 106101, 2014.

[21] Remmler, S., and Hickel, S., "Direct and large eddy simulation of stratified turbulence," *International Journal of Heat and Fluid Flow*, Vol. 35, 2012, pp. 13–24.

[22] Kaller, T., Pasquariello, V., Hickel, S., and Adams, N., "Large-eddy simulation of the high-Reynolds-number flow through a high-aspect-ratio cooling duct," *Proceedings of the 10th International Symposium on Turbulence and Shear Flow Phenomena (TSFP-10), Chicago, USA*, 2017.

[23] Rochlitz, H., Scholz, P., and Fuchs, T., "The flow field in a high aspect ratio cooling duct with and without one heated wall," *Experiments in Fluids*, Vol. 56, No. 12, 2015, pp. 1–13.

[24] Lee, J., Jung, S. Y., Sung, H. J., and Zaki, T. A., "Effect of wall heating on turbulent boundary layers with temperature-dependent viscosity," *Journal of Fluid Mechanics*, Vol. 726, 2013, pp. 196–225.

[25] Zonta, F., Marchioli, C., and Soldati, A., "Modulation of turbulence in forced convection by temperature-dependent viscosity," *Journal of Fluid Mechanics*, Vol. 697, 2012, pp. 150–174.

[26] Kays, W. M., "Turbulent Prandtl Number - Where Are We?" *Journal of Heat Transfer*, Vol. 116, No. 2, 1994, pp. 284–295.

[27] Kang, S., and Iaccarino, G., "Computation of turbulent Prandtl number for mixed convection around a heated cylinder," *Annual Research Briefs, Center of Turbulence Research, Stanford University*, 2010, pp. 295–304.

[28] Hirota, M., Fujita, H., Yokosawa, H., Nakai, H., and Itoh, H., "Turbulent heat transfer in a square duct," *International Journal of Heat and Fluid Flow*, Vol. 18, No. 1, 1997, pp. 170–180.